



Remarkable improvement of the turn-on characteristics of a Fe_2O_3 photoanode for photoelectrochemical water splitting with coating a FeCoW oxy-hydroxide gel

Jingran Xiao, Huali Huang, Qiuyang Huang, Xiang Li, Xuelan Hou, Le Zhao, Rui Ma, Hong Chen¹, Yongdan Li*

Collaborative Innovation Center of Chemical Science and Engineering (Tianjin), Tianjin Key Laboratory of Applied Catalysis Science and Technology, State Key Laboratory of Chemical Engineering (Tianjin University), School of Chemical Engineering, Tianjin University, Tianjin 300072, China



ARTICLE INFO

Article history:

Received 31 December 2016

Received in revised form 21 April 2017

Accepted 27 April 2017

Available online 28 April 2017

Keywords:

Hematite

Turn-on voltage

Photoanode

Water splitting

ABSTRACT

A FeCoW oxy-hydroxide gel coated Fe_2O_3 film photoanode has been examined for photoelectrochemical (PEC) water oxidation reaction. The FeCoW coating acts as a hole storage layer, resulting in efficient hole extraction from Fe_2O_3 for water oxidation. In addition, the surface state of FeCoW/ Fe_2O_3 shifts to higher position, thus allows for a lower turn-on voltage (V_{on}) of the photocurrent. The composite anode exhibits an 84% increase of the photocurrent, at 1.23 V versus reversible hydrogen electrode (RHE), over the bare Fe_2O_3 photoanode. The V_{on} is as low as 0.67 V vs. RHE. The applied bias photon-to-current efficiency of the composite is 2.7 times higher than that of the bare Fe_2O_3 . Moreover, an extremely low bias photoresponse of 0.45 V vs. RHE and a good stability are observed with the FeCoW/ Fe_2O_3 photoanode. Besides, with changing of the thickness of the FeCoW coating slurry, the PEC performance of the FeCoW/ Fe_2O_3 photoanode can be tuned.

© 2017 Elsevier B.V. All rights reserved.

1. Introduction

Due to the increased concern of energy supply and environmental issues, photoelectrochemical (PEC) water splitting becomes a challenging research topic in the field of sustainable energy. A smart design of PEC cell has two major counterparts, i.e. the photoanode for water oxidation and the photocathode for water reduction. As a multi-electron transfer process, the water oxidation at the photoanode has been one of the major bottlenecks for the overall PEC efficiency [1]. Among the intensively explored photoanode materials, hematite (Fe_2O_3) stands out with its broad light spectrum absorption, durability in water, and natural abundance [2]. With a suitable band-gap of 2.0–2.2 eV, its theoretical solar energy conversion efficiency was predicted in the range of 12.7–16.8% [3,4]. Nevertheless, due to the short hole-diffusion length (2–4 nm), and the sluggish water oxidation kinetics on the surface, Fe_2O_3 suffers

from a low photo responsive current and a high turn-on voltage which limit the energy conversion efficiency [5].

One of the approaches to improve the Fe_2O_3 anode efficiency is to incorporate an oxygen evolution reaction (OER) catalyst [6,7]. Many OER catalysts, e.g. group 8–10 metal oxides, hydroxides and phosphates, have shown promoting effects in the PEC performance of Fe_2O_3 [8–12]. In general, an OER catalyst enhances the performance in two ways, viz., extracts holes from Fe_2O_3 phase thus enhancing the photocurrent, and shifts the surface state to a higher position accordingly facilitating a lower turn-on voltage (V_{on}) of the photocurrent. However, the catalysts tested are often not efficient on both sides. For instance, IrO_2 is inefficient to draw holes from Fe_2O_3 [9], while Co_3O_4 shows very limited contribution to shift the V_{on} of the photocurrent [13]. Meanwhile, the stability and cost of the OER catalyst are also crucial factors. With meeting both the two requirements mentioned, cobalt-phosphate (Co-Pi) was regarded as one of the most promising cocatalysts for Fe_2O_3 photoanode. A recently discovered FeCoW oxy-hydroxide gel OER catalyst exhibited an exceptionally low over-potential, i.e. 191 mV at 10 mA cm^{−2} in alkaline electrolyte, as well as a good stability [14].

Herein, we present a successful effort using the FeCoW oxy-hydroxide as a surface promoter of the Fe_2O_3 photoanode in

* Corresponding author.

E-mail address: ydli@tju.edu.cn (Y. Li).

¹ School of Environmental Science and Engineering, Tianjin University, Tianjin 300072, China.

water splitting. The FeCoW OER catalyst acts as an efficient and stable promoter simultaneously increasing the photocurrent with capturing the holes and decreasing the V_{on} with raising the location of the surface state.

2. Experimental

2.1. Materials synthesis

The Fe_2O_3 film grown on fluorine-doped tin oxide (FTO) substrate was synthesized through a hydrothermal procedure reported previously [15,16]. In detail, 0.09 M ferric chloride and 0.1 M of sodium nitrate were dissolved in 25 mL deionized water. After filtration, the solution at $\text{pH} = 1.4$ (adjusted by HCl) was transferred to a 50 mL Teflon-lined stainless steel autoclave. FTO glass was immersed upside-down in the autoclave and heated at 95 °C for 4 h. After growth, the obtained yellow film was calcined at 550 °C for 2 h and further annealed at 800 °C for 20 min. The Fe_2O_3 electrode with active area of $1 \times 1 \text{ cm}^2$ was prepared after cooling to room temperature.

The synthesis procedure of the FeCoW oxy-hydroxide gel catalyst is consistent with literature [14]. Typically, to form the FeCoW ink, 3 mg of FeCoW powder was dispersed in 1 mL mixture of water and ethanol (4:1, v/v), and then 80 μL of Nafion solution (5 wt.% in water) was added. The suspension with estimated concentration of 3 mg mL^{-1} was ultrasonically treated for 2 h. The FeCoW/ Fe_2O_3 films were prepared by spin-coating with the FeCoW suspension onto the Fe_2O_3 film at 3000 rpm for 30 s. The number of spin coating times was controlled for varying the thicknesses of the FeCoW layer. A number of FeCoW concentrations of the suspension (1, 3, 5 and 10 mg mL^{-1}) were examined for different FeCoW loading amount with the same spin speed and time.

A $\text{Co}_3\text{O}_4/\text{Fe}_2\text{O}_3$ sample was prepared via a hydrothermal process [17]. 0.40 mL of 25% $\text{NH}_3 \cdot \text{H}_2\text{O}$ was added into 25.0 mL of 5 mM $\text{Co}(\text{CH}_3\text{COO})_2 \cdot 4\text{H}_2\text{O}$ ethanol solution under vigorous stirring. After stirring for 10 min, the obtained brown sol was transferred into a Teflon-lined autoclave reactor with Fe_2O_3 photoanode inside and hydrothermally treated at 120 °C for 1 h. After cooled down to room temperature naturally, the obtained $\text{Co}_3\text{O}_4/\text{Fe}_2\text{O}_3$ anode was then washed and dried.

The $\text{Co-Pi}/\text{Fe}_2\text{O}_3$ sample was prepared with a photoassisted electrodeposition technique [18]. 0.5 mM $\text{Co}(\text{NO}_3)_2$ was dissolved in a buffer of 0.1 M KH_2PO_4 adjusting to pH 7 with 1 M NaOH as the electrolyte. The deposition was carried out at +0.2 V vs. Ag/AgCl for 5 min with simulated sunlight illumination (100 mW cm^{-2}).

The $\text{FeOOH}/\text{Fe}_2\text{O}_3$ sample was prepared via a dip coating process, i.e., the Fe_2O_3 anode was immersed in a 5 mM $\text{FeCl}_2 \cdot 4\text{H}_2\text{O}$ aqueous solution at 40 °C for 10 min followed by washing and drying [19].

2.2. Photoelectrochemical measurements

The photocurrent was recorded with an electrochemical workstation (CHI 660B, CH Instrument, Chenzhua, Shanghai) using a three-electrode configuration with Ag/AgCl as the reference electrode, Pt sheet ($1 \times 1 \text{ cm}^2$) as the counter electrode and 1.0 M NaOH (70 mL, pH 13.6) as the electrolyte which is contained in a quartz reactor with a volume of 150 mL. The polarization curves were scanned at 20 mV s^{-1} under filtered AM 1.5G simulated sunlight from a 300 W xenon lamp (Perfect Light, PLS-SXE-300). The light intensity was measured as 100 mW cm^{-2} using a radiometer (Sanpometer SM206). If not otherwise specified, the anodes were illuminated from the back-side. Transient chronoamperometry was performed with sample interval of 0.001 s. EIS measurements under AM 1.5G illumination were carried out in a frequency from

100 kHz to 1 Hz with applying amplitude of 20 mV at different applied bias. All potentials were referenced to the reversible hydrogen electrode (RHE) with the Nernst equation [20]:

$$V_{\text{RHE}}(\text{V}) = V_{\text{Ag}/\text{AgCl}}(\text{V}) + 0.1976 + 0.059 \text{ pH}$$

The applied bias photo-to-current conversion efficiency (ABPE) was calculated by the following equation [21]:

$$\text{ABPE} = \frac{J \times (1.23 - |V_{\text{RHE}}|)}{P} \times 100\%$$

where J is the photocurrent density (mA cm^{-2}) at the applied bias V vs. RHE, and P is the incident light intensity (mW cm^{-2}).

The produced H_2 and O_2 were collected and measured. The reactor was previously purged with N_2 for 30 min to eliminate the dissolved oxygen and the air in the reactor. After reaction at 1.23 V vs. RHE, H_2 and O_2 were carried out by continuous N_2 flow (20 mL min^{-1}) and collected with a gas sampling bag. For each sampling with an interval of 30 min, 1 mL gas was pumped out with a chromatography needle and injected in the gas chromatograph (GC, Agilent 6890D, TCD detector, molecular sieve 5A column, carrier gas (Ar) flow rate of 36 mL min^{-1} , oven temperature of 50 °C and detector temperature of 120 °C). The amounts of H_2 and O_2 were calculated with N_2 as a reference.

2.3. Characterization

The X-ray diffraction patterns (XRD) were collected from 20° to 70° at a speed of 8° min^{-1} with a Bruker AXS, D8-S4 powder diffractometer with Cu Ka illumination (40 kV \times 200 mA). The SEM images were recorded using a Hitachi S-4800 field emission scanning electron microscope. The TEM and high-resolution TEM micrographs were examined by a transmission electron microscope (TEM, JEM-2100F). The UV-visible (UV-vis) diffuse reflection characteristic was obtained with the diffuse reflection method on a PerkinElmer L750 spectrometer. The X-ray photoelectron spectroscopy (XPS) measurement was detected with an ESCA PHI 1600 instrument using an Mg K α X-ray source for excitation. The C 1s binding energy at 284.6 eV is used for spectrum calibration.

3. Results and discussion

3.1. Material characterization

The FeCoW suspension was synthesized via a sol-gel technique. The elemental mapping results in Fig. 1 confirm a uniform distribution of Fe, Co, W and O elements in the dried FeCoW powder. As indicated from the XRD patterns in Fig. 2, the samples exhibit a typical crystal structure of $\alpha\text{-Fe}_2\text{O}_3$ (JCPDS No. 33-0664) with an oriented growth of (110) plane. The FeCoW coating showed no impact on the crystal structure or the crystallinity of Fe_2O_3 . The morphologies of the photoanode materials recorded with SEM and TEM images are illustrated in Fig. 3. The FeOOH sample, shown in the insert of Fig. 3a, displays a porous surface. After annealing at 800 °C, the Fe_2O_3 film shows slight sintering with higher porosity (Fig. 3a). After coating of the FeCoW gel via a spin-coating technique, the surface of the Fe_2O_3 film becomes rough, as shown in Fig. 3b. The FeCoW/ Fe_2O_3 composite displays a uniform morphology in the low magnification image in Fig. 3c. A full coverage of a FeCoW layer on Fe_2O_3 is confirmed by the TEM image (Fig. 3f). As observed in the HRTEM micrograph, a thin disorder layer is seen on the bare Fe_2O_3 (Fig. 3d), while a much thicker amorphous layer of FeCoW is observed on the surface of FeCoW/ Fe_2O_3 (Fig. 3e). The thickness of the FeCoW overlayer is measured to be about 2 nm by subtracting the thickness of the disorder layer.

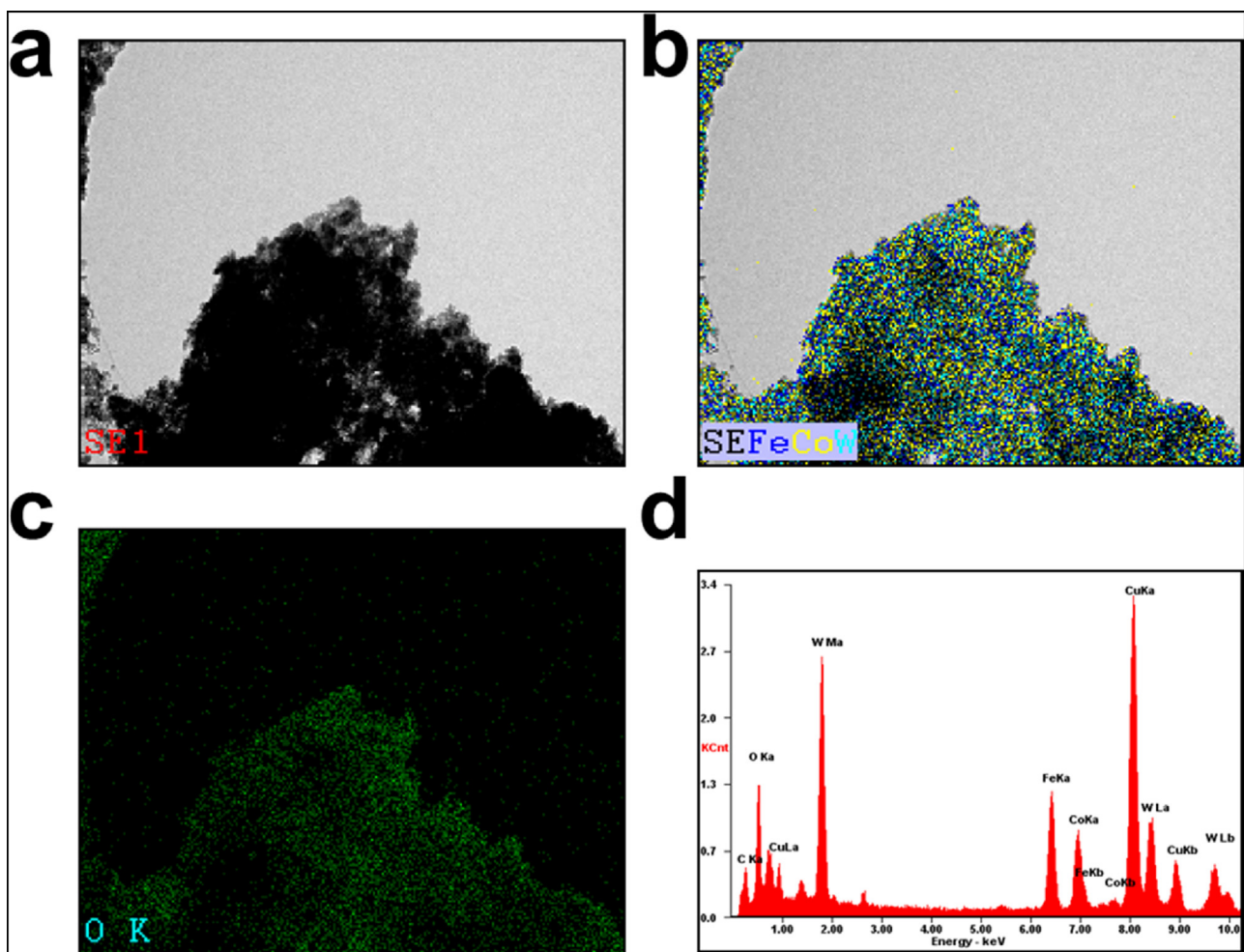


Fig. 1. (a) TEM micrograph of the FeCoW sample, EDX mapping of (b) the mixed Fe, Co and W elements, (c) O element and (d) EDX element distribution of the FeCoW powder.

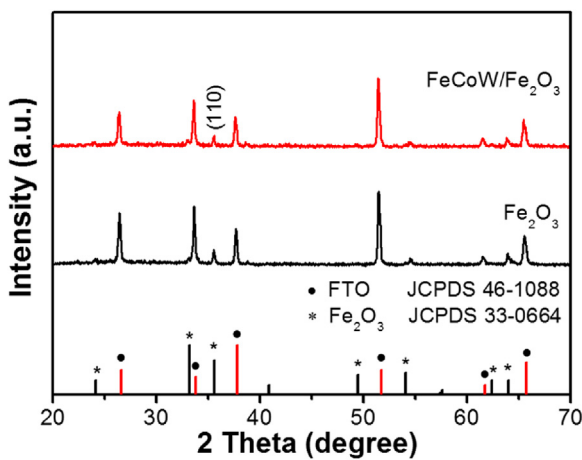


Fig. 2. XRD patterns of the Fe₂O₃ and FeCoW/Fe₂O₃ samples.

The XPS spectra of the O 1s region were obtained from vacuum dried Fe₂O₃ and FeCoW/Fe₂O₃ surfaces, as depicted in Fig. 4a. The O 1s spectrum of Fe₂O₃ shows as convoluted double peaks which are assigned to the lattice and hydroxyl oxygen, respectively [22]. Notably, the binding energy of the lattice oxygen in FeCoW/Fe₂O₃ broadens and shows a 0.9 eV shift to the higher end from that of Fe₂O₃, and becomes higher than that of the Co–O, but still lower than that of the W=O bond [23,24], which is due to the coexistence

of lattice oxygen bonding with the three metal atoms. In addition, the much stronger hydroxyl O 1s peak in FeCoW/Fe₂O₃ is attributed to the hydroxylated surface of the FeCoW layer. Besides, the additional peak at 535.8 eV is speculated to be the oxygen in the ether configuration brought from Naion solution [25]. The UV-vis diffuse reflection spectra of the Fe₂O₃, FeCo/Fe₂O₃ and FeCoW/Fe₂O₃ samples are given in Fig. 4b. The difference of the UV-vis absorption characteristic between the bare and the composite samples is very slight, indicating no additional photoresponse induced by the coating of a FeCo or FeCoW layer.

3.2. Photoelectrochemical performance

The promotion effect of the FeCoW layer on the Fe₂O₃ photoanode is examined by measuring the polarization curve at a scan rate of 20 mV s⁻¹ under standard simulated AM 1.5 G irradiation in 1 M NaOH electrolyte, as given in Fig. 5a. A reference sample FeCo oxy-hydroxide coated Fe₂O₃, which was synthesized similarly as the FeCoW/Fe₂O₃ is also measured. The turn-on voltages are derived with a Butler plot, shown as Fig. 5b, where the V_{on} shifted to cathode side by 100 mV (from 0.84 V to 0.74 V) and by 170 mV (from 0.84 V to 0.67 V) for the FeCo and FeCoW coated samples, respectively. Likewise, the photocurrent density shows a substantial increase from 0.64 to 1.04 and further to 1.18 mA cm⁻² at 1.23 vs. RHE. The applied bias photon-to-current efficiency (ABPE) is calculated with the data derived from the polarization curve with assuming a 100% Faradaic efficiency (Fig. 5c). The maxi-

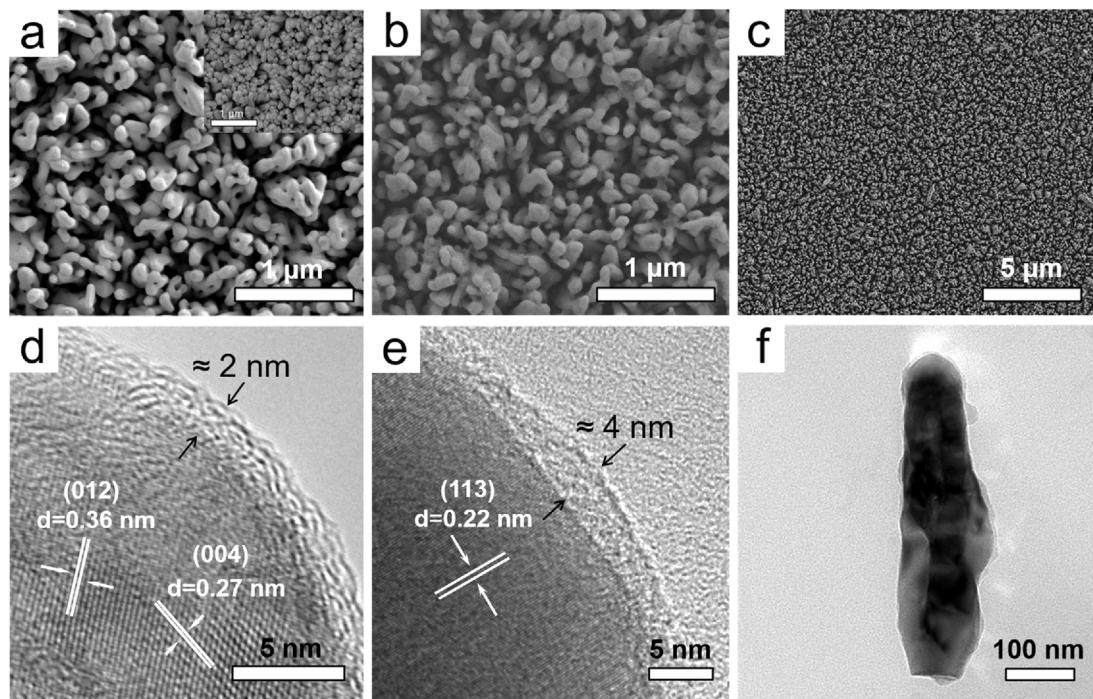


Fig. 3. (a) SEM images of Fe₂O₃, insert is the SEM image of the FeOOH sample; (b, c) FeCoW/Fe₂O₃ photoanodes. HRTEM images of (d) bare Fe₂O₃ and (e) FeCoW/Fe₂O₃ surface. (f) TEM image of a FeCoW/Fe₂O₃ nanowire.

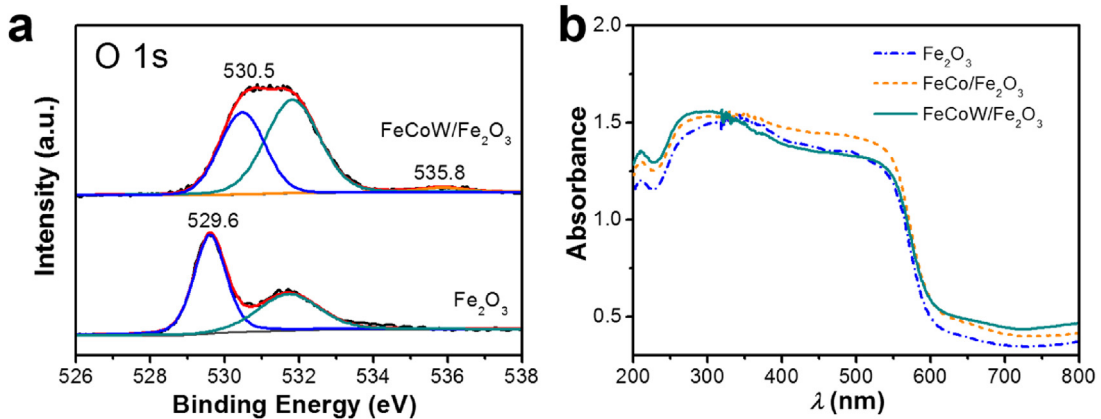


Fig. 4. (a) High-resolution XPS spectra of the O 1s region from vacuum dried Fe₂O₃ and FeCoW/Fe₂O₃ surfaces. (b) UV-vis diffuse reflection spectra of the Fe₂O₃, FeCo/Fe₂O₃ and FeCoW/Fe₂O₃ samples.

imum ABPE of the FeCo/Fe₂O₃ anode achieves 0.12%, which is twice of that of the non-promoted Fe₂O₃ of 0.06%. The FeCoW/Fe₂O₃ anode gives a further enhanced maximum ABPE of 0.16%, meanwhile, the voltage at the maximum ABPE also shifts to cathode side by 0.07 V. Further low voltage was applied to the photoanode (Fig. 5d) and a significant photoresponse is observed at around 0.45 V for the FeCoW/Fe₂O₃ sample, which is impressive, since the theoretically necessary bias is 0.3–0.4 V for Fe₂O₃ to initiate the water splitting reaction [26]. In contrast, FeCo does not show an obvious improvement of the low bias performance.

Long-term photocurrent density under continuous illumination was measured to test the photostability of the FeCoW/Fe₂O₃ photoanode, as given in Fig. 6a. A slight decay during 20 h of photoelectrolysis run at 1.23 V vs. RHE was observed. After the renewal of the electrolyte, the PEC performance shows a complete recovery (Fig. 6b). The outstanding stability is attributed to the strong adhesion of the superbly stable FeCoW catalyst on Fe₂O₃ in the alkaline solution.

The H₂ and O₂ gases generated in 3 h from the Fe₂O₃, FeCo/Fe₂O₃ and FeCoW/Fe₂O₃ photoanodes were collected and quantified (Fig. 6c). For all the samples, the ratio of evolved O₂ and H₂ is around 2.1. The slight discrepancy with stoichiometry is probably due to the inevitable O₂ dissolution. The H₂ and O₂ evolution amounts were increased with FeCo coating and further enhanced by FeCoW coating, which is consistent with the photocurrent results. The Faraday efficiency of the O₂ evolution reaction for the samples is identical and is determined to be 90–94% after the system reaches a steady state. Thus, the photogenerated holes were utilized for O₂ production in the system.

A number of FeCoW/Fe₂O₃ samples with changing the thickness of the FeCoW coating slurry and the number of coatings were prepared and examined. The polarization curves are presented in Fig. 7. Substantially, the increase of the FeCoW gel thickness corresponds to an increased photocurrent but the turn-on voltages are almost the same. However, increase of the FeCoW coating layers leads to a negative effect on both the photocurrent value and

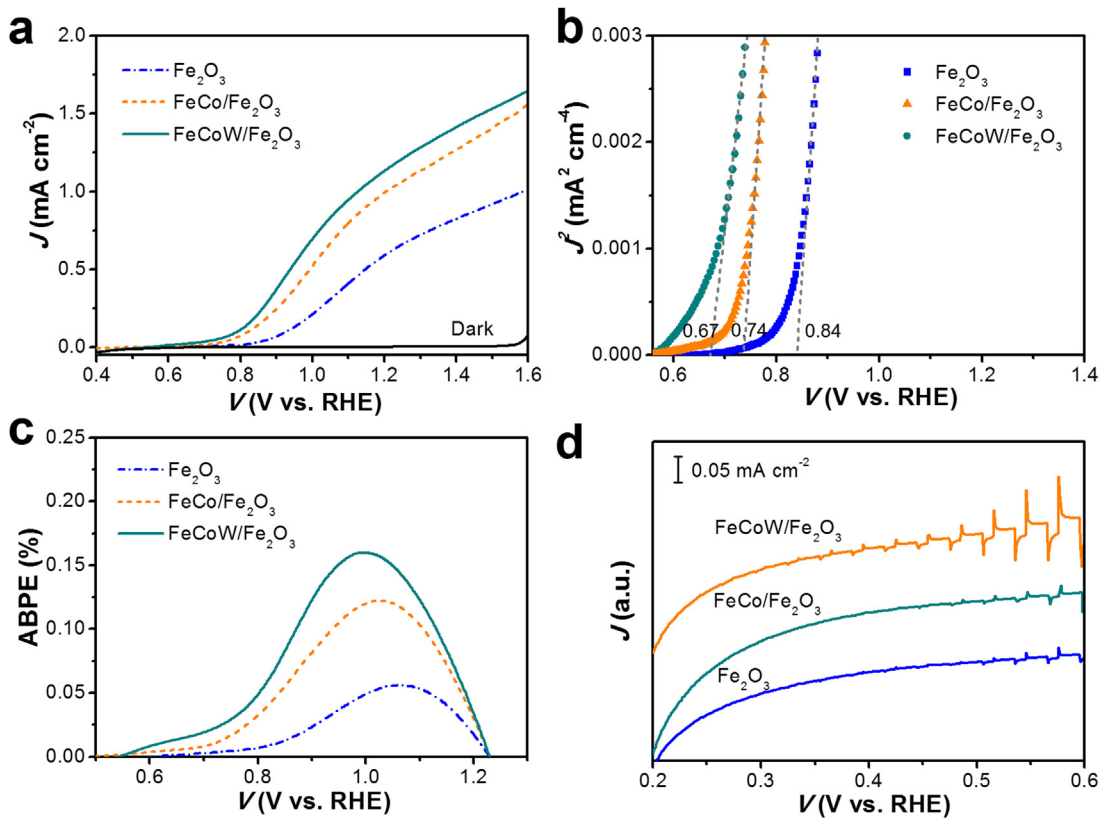


Fig. 5. (a) Respective polarization curves, (b) Butler plots, (c) Applied bias photon-to-current conversion efficiency (ABPE) and (d) Low-bias polarization curves for the Fe_2O_3 , $\text{FeCo}/\text{Fe}_2\text{O}_3$ and $\text{FeCoW}/\text{Fe}_2\text{O}_3$ photoanodes. The turn-on voltage is derived from the Butler plots as the value at which the extrapolation of the linear relationship between J^2 and V intercepts with $J^2 = 0$.

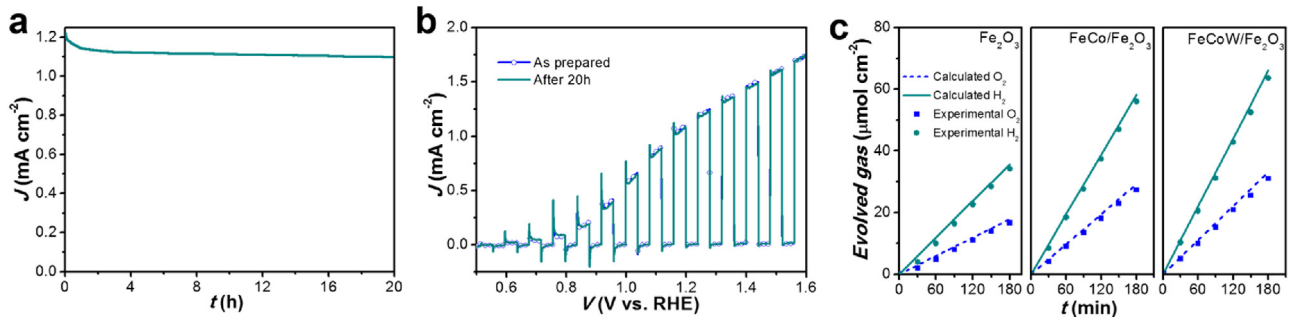


Fig. 6. (a) Long-term chronoamperometry of the $\text{FeCoW}/\text{Fe}_2\text{O}_3$ photoanode at 1.23 vs. RHE, (b) Polarization curves of the as prepared and long-term tested $\text{FeCoW}/\text{Fe}_2\text{O}_3$ photoanode in fresh electrolyte, (c) Evolution of H_2 and O_2 gases from the Fe_2O_3 , $\text{FeCo}/\text{Fe}_2\text{O}_3$ and $\text{FeCoW}/\text{Fe}_2\text{O}_3$ photoanodes at 1.23 V vs. RHE with comparison to the gas evolutions estimated from the current generation.

the turn-on voltage. These results suggest that thin layer coating of FeCoW effectively promotes the PEC performance of Fe_2O_3 and with the increase of the thickness of the FeCoW coating slurry, the promotion effect is enhanced in a range.

A number of OER catalysts, i.e., FeOOH , Co_3O_4 and Co-Pi , loaded Fe_2O_3 samples, those showed good PEC performance and photo-stability in recent reports, were also prepared as references. The comparison of the polarization curves for the samples is presented in Fig. 8. The OER catalysts show different promotion effects on the photocurrent response of Fe_2O_3 . Regardless of the bare Fe_2O_3 , the $\text{FeOOH}/\text{Fe}_2\text{O}_3$ anode shows the lowest photocurrent among them. The $\text{Co}_3\text{O}_4/\text{Fe}_2\text{O}_3$ anode exhibits a similar performance with $\text{FeCo}/\text{Fe}_2\text{O}_3$. Particularly, the turn-on voltage of $\text{FeCoW}/\text{Fe}_2\text{O}_3$ anode is as low as the well-known $\text{Co-Pi}/\text{Fe}_2\text{O}_3$. Most significantly,

the $\text{FeCoW}/\text{Fe}_2\text{O}_3$ anode shows even higher photocurrent than that of $\text{Co-Pi}/\text{Fe}_2\text{O}_3$ when the bias is above 0.85 V.

3.3. Photoelectrochemical characterization

The electrochemical impedance spectra (EIS) of the electrode samples under AM 1.5 G illumination were also measured. The equivalent circuit (EC) for interpreting the EIS data is proposed and illustrated in Fig. 9a, which consists of a couple of capacitances and resistances in parallel [27,28]. The representative Nyquist plots at 1.0 V under illumination are presented in Fig. 9b. Each curve composes two semicircles. The semicircle at high frequency is related to the charge transfer resistance in the bulk, and the one at low frequency ascribes to the charge transfer resistance at the

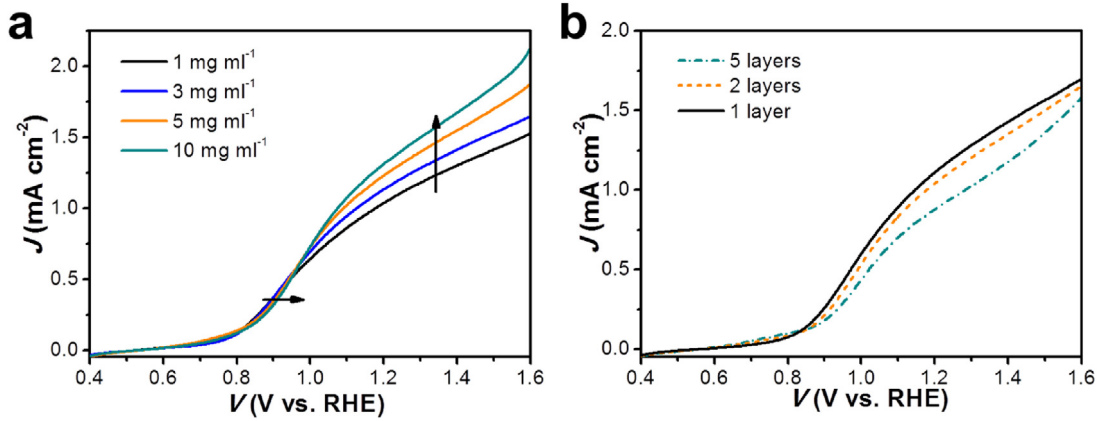


Fig. 7. Polarization curves of the FeCoW/Fe₂O₃ photoanodes prepared with spin-coating with (a) changed FeCoW suspension concentrations at a spin-coating speed of 3000 rpm and (b) changed spin-coating times at a speed of 3000 rpm with 3 mg ml⁻¹ FeCoW suspension.

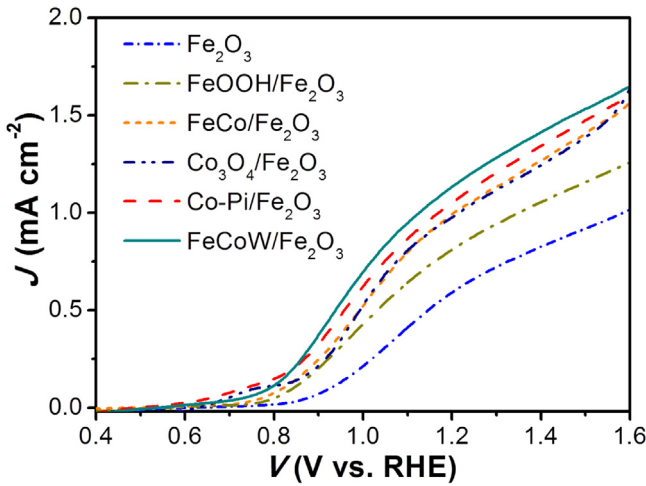


Fig. 8. Comparison of the polarization curves of the Fe₂O₃, FeOOH/Fe₂O₃, FeCo/Fe₂O₃, Co₃O₄/Fe₂O₃, Co-Pi/Fe₂O₃ and FeCoW/Fe₂O₃ photoanode samples.

anode/electrolyte interface [29]. The diameter of the second semi-circle of the FeCoW/Fe₂O₃ sample is smaller than that of FeCo/Fe₂O₃ and much smaller than that of the Fe₂O₃. The values of $R_{ct,bulk}$ of the FeCo/Fe₂O₃ and FeCoW/Fe₂O₃ anodes are quite similar to each other and are both small, in the order of 10^2 – 10^3 Ω cm² (Fig. 10a), indicating the fast hole transfer from the valence band (VB) of Fe₂O₃

to the coating layers. Klahr et al. [30] examined the Co-Pi coated hematite with similar $R_{ct,bulk}$ values and proposed these resistances are consistent with having fast charge transfer of holes from the VB of hematite to the Co-Pi. The values of the trap capacitance (C_{trap}) improve significantly with the coating of the promoters (Fig. 10b), and FeCoW shows a much profound effect than that of FeCo. The increase of the C_{trap} values means the improvement of the hole capture and storage capability of the anode material [31], suggesting that the FeCoW coating behaves as a hole storage layer to extract holes from Fe₂O₃. Meanwhile, the $R_{ct,trap}$ value, reversely correlated to the rate of hole transfer from the solid surface to the adsorbed water molecule, decreases with the order uncoated, FeCo coated and FeCoW coated Fe₂O₃ (Fig. 10c) for the three samples. The decrease of $R_{ct,trap}$ indicates the decrease of the recombination ratio of the surface electron–hole pairs, thus resulting in the acceleration of the surface water oxidation reaction [9,32]. For the three samples, the V_{on} is correlated coincidentally with the peak location of the C_{trap} , indicating that the reaction is controlled predominantly by the hole transfer at the interface. As confirmed by the higher C_{trap} and lower $R_{ct,trap}$ values, FeCoW exhibits a better catalytic effect than FeCo does.

The capturing effect of holes by FeCo and FeCoW catalysts is more intuitively reflected in the Bode plots of the anodes. The higher of the phase value reflects the more accumulation of charge at a certain interface [33]. The Bode plots of the Fe₂O₃, FeCo/Fe₂O₃ and FeCoW/Fe₂O₃ electrodes at three representative applied potentials are presented in Fig. 11. At 0.7 V all the examined electrodes

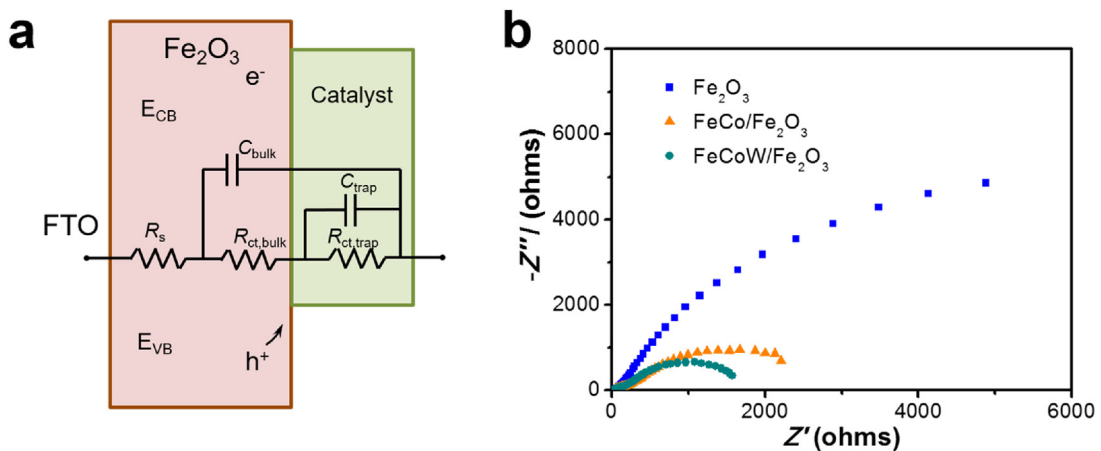


Fig. 9. (a) Equivalent circuit used for interpretation of the hematite electrodes loaded with an OER catalyst. (b) Nyquist plots of the Fe₂O₃, FeCo/Fe₂O₃ and FeCoW/Fe₂O₃ photoanodes under AM 1.5 illumination.

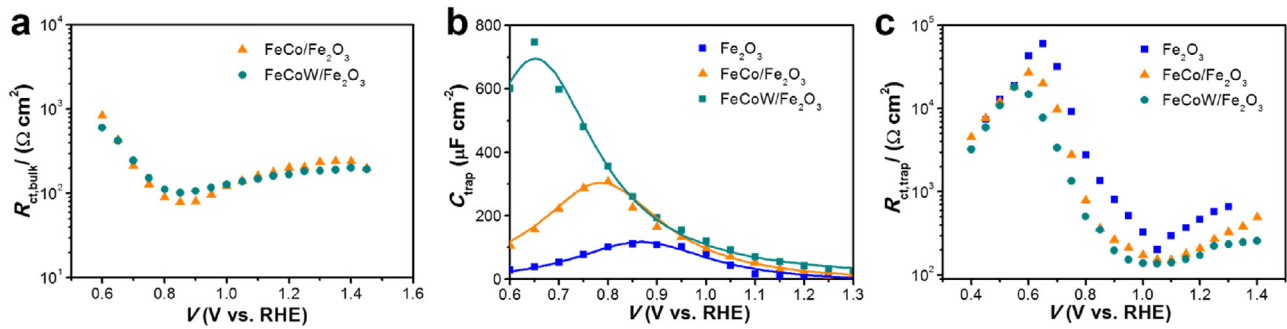


Fig. 10. (a) $R_{ct,bulk}$, (b) C_{trap} and (c) $R_{ct,trap}$ fitting plots from EIS response of the Fe_2O_3 , $\text{FeCo/Fe}_2\text{O}_3$ and $\text{FeCoW/Fe}_2\text{O}_3$ photoanodes under AM 1.5 illumination.

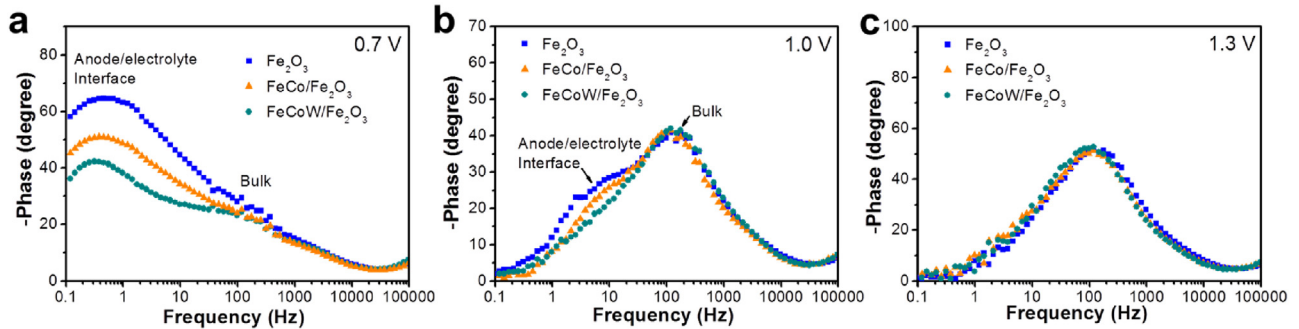


Fig. 11. Bode plots of the Fe_2O_3 , $\text{FeCo/Fe}_2\text{O}_3$ and $\text{FeCoW/Fe}_2\text{O}_3$ electrodes at (a) 0.7 V, (b) 1 V and (c) 1.3 V.

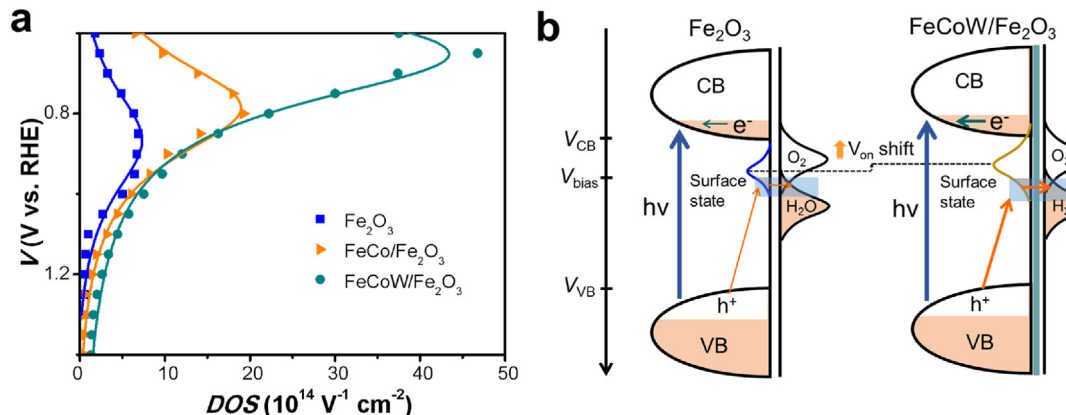


Fig. 12. (a) Applied voltage versus densities of surface states (DOS) of the electrodes. Solid lines correspond to Lorentzian fit results. (b) Proposed kinetic scheme of the hole transfer pathways from the VB of Fe_2O_3 to the surface states for the Fe_2O_3 and $\text{FeCoW/Fe}_2\text{O}_3$ photoanodes under illumination at a bias of 1.0 V vs. RHE. Shaded and blank areas represent electron filled or empty states, respectively.

showed two characteristic peaks centered at around 0.4 and 170 Hz (Fig. 11a). The low frequency peak of the electrodes shows much higher phase value, suggesting that the water oxidation is limited by charge transfer at the anode/electrolyte interface at this potential. The low frequency peak of $\text{FeCoW/Fe}_2\text{O}_3$ electrodes is much lower than that of bare Fe_2O_3 , suggesting that part of holes trapped in the surface state is captured by the FeCoW layer for water oxidation. At 1.0 V in Fig. 11b, the high frequency peak of the bare Fe_2O_3 becomes much larger and the low frequency peak is reduced, suggesting that at this potential the surface reaction was predominantly limited by bulk transfer of holes. By contrast, the low frequency peak of $\text{FeCoW/Fe}_2\text{O}_3$ electrode almost disappeared, indicating the holes trapped in the surface state of Fe_2O_3 are totally captured by the FeCoW layer. At 1.3 V in Fig. 11c, the low frequency peaks of the three electrodes all disappeared, leaving only one peak visible. At this potential, which is higher than the thermo-

dynamic potential of water splitting (1.23 V), the water oxidation is only limited by the intrinsic properties of the Fe_2O_3 , and thus the bare and promoted anodes reveal similar bode plots.

The density of surface state (DOS) is extracted from the C_{trap} plots ($C_{trap} = q \times \text{DOS}$, Fig. 12a) [34]. A kinetic scheme of the hole transfer pathways from the VB of Fe_2O_3 to the surface states for the Fe_2O_3 and $\text{FeCoW/Fe}_2\text{O}_3$ photoanodes at 1.0 V vs. RHE is proposed, illustrated as Fig. 12b. For both photoanodes, the surface states locate inside the band-gap and the hole transfers from the top of the VB of Fe_2O_3 . The V_{on} of the photocurrent occurs when half of the surface states are emptied, so that, for the FeCoW coated Fe_2O_3 , the surface state locates energetically higher, allowing for a lower V_{on} of the photocurrent [27]. On the other hand, the hole transfer rate and the corresponding photocurrent depend on the overlapping (light blue shade) between the filled surface states and the filled redox couple states (H_2O) [35]. Hence, at a certain polarization

voltage, the FeCoW/Fe₂O₃ photoanode provides a higher available filled surface state and thus leads to an increased photocurrent.

4. Conclusion

Here, we showed that a thin layer of FeCoW coating displays a profound promoting effect on the performance of a Fe₂O₃ photoanode.

As evidenced from the EIS Bode and Nyquist plots, the FeCoW layer collects and stores the photogenerated holes from the Fe₂O₃ electrode under illumination, thus accelerating charge separation and inhibiting surface recombination. FeCoW coating also shifts the surface state to higher location which allows for a lowered V_{on} .

The V_{on} is confirmed to shift to the cathode side by 170 mV and the photocurrent is increased by 84% at 1.23 V vs. RHE for the FeCoW coated sample over the bare Fe₂O₃ photoanode. In addition, it is impressive that the FeCoW/Fe₂O₃ composite photoanode achieves an extraordinarily low bias photoresponse at a voltage of 0.45 V. Furthermore, the composite photoanode exhibits an excellent stability during 20 h illumination. Moreover, with regulating the thickness of the FeCoW coating slurry, the promotion effect on the PEC performance of Fe₂O₃ can be further tuned.

The promoting effect of the FeCoW oxyhydroxide gel on the turn-on characteristics and photocurrent performance of the Fe₂O₃ photoanode is confirmed to be much stronger than that of FeOOH or Co₃O₄ OER catalysts. The turn-on characteristics of the FeCoW/Fe₂O₃ is comparable to that of the Co-Pi catalyst. Moreover, the photocurrent of the FeCoW/Fe₂O₃ is slightly higher than that of the Co-Pi/Fe₂O₃ photoanode.

Acknowledgements

This work has been supported in part by the Program of Introducing Talents to the University Disciplines under file number B06006, and the Program for Changjiang Scholars and Innovative Research Teams in Universities under file number IRT 0641.

References

- [1] S.M. Sun, W.Z. Wang, D.Z. Li, L. Zhang, D. Jiang, *ACS Catal.* 4 (2014) 3498–3503.
- [2] Y. Zhang, H. Zhang, H. Ji, W. Ma, C. Chen, J. Zhao, *J. Am. Chem. Soc.* 138 (2016) 2705–2711.
- [3] Y.J. Lin, G.B. Yuan, S. Sheehan, S. Zhou, D.W. Wang, *Energy Environ. Sci.* 4 (2011) 4862–4869.
- [4] Gurudayal, D. Sabba, M.H. Kumar, L.H. Wong, J. Barber, M. Graetzel, N. Mathews, *Nano Lett.* 15 (2015) 3833–3839.
- [5] I.S. Cho, H.S. Han, M. Logar, J. Park, X. Zheng, *Adv. Energy Mater.* 6 (2016) 1501840.
- [6] K. Sun, N. Park, Z. Sun, J. Zhou, J. Wang, X. Pang, S. Shen, S.Y. Noh, Y. Jing, S. Jin, P.K.L. Yu, D. Wang, *Energy Environ. Sci.* 5 (2012) 7872–7877.
- [7] P. Liao, J.A. Keith, E.A. Carter, *J. Am. Chem. Soc.* 134 (2012) 13296–13309.
- [8] W.D. Chemelewski, H.-C. Lee, J.-F. Lin, A.J. Bard, C.B. Mullins, *J. Am. Chem. Soc.* 136 (2014) 2843–2850.
- [9] Z. Wang, G. Liu, C. Ding, Z. Chen, F. Zhang, J. Shi, C. Li, *J. Phys. Chem. C* 119 (2015) 19607–19612.
- [10] D.K. Zhong, J. Sun, H. Inamaru, D.R. Gamelin, *J. Am. Chem. Soc.* 131 (2009) 6086–6087.
- [11] Z. Hu, Z. Shen, J.C. Yu, *Chem. Mater.* 28 (2016) 564–572.
- [12] Q. Li, J. Bian, N. Zhang, D.H.L. Ng, *Electrochim. Acta* 155 (2015) 383–390.
- [13] L. Xi, P.D. Tran, S.Y. Chiam, P.S. Bassi, W.F. Mak, H.K. Mulpudi, S.K. Batabyal, J. Barber, J.S.C. Loo, L.H. Wong, *J. Phys. Chem. C* 116 (2012) 13884–13889.
- [14] B. Zhang, X. Zheng, O. Vozny, R. Comin, M. Bajdich, M. García-Melchor, L. Han, J. Xu, M. Liu, L. Zheng, F.P. García de Arquer, C.T. Dinh, F. Fan, M. Yuan, E. Yassitepe, N. Chen, T. Regier, P. Liu, Y. Li, P. De Luna, A. Jammohamed, H.L. Xin, H. Yang, A. Vojvodic, E.H. Sargent, *Science* 352 (2016) 333–337.
- [15] Y. Ling, G. Wang, D.A. Wheeler, J.Z. Zhang, Y. Li, *Nano Lett.* 11 (2011) 2119–2125.
- [16] Y. Zhang, S. Jiang, W. Song, P. Zhou, H. Ji, W. Ma, W. Hao, C. Chen, J. Zhao, *Energy Environ. Sci.* 8 (2015) 1231–1236.
- [17] G. Liu, J. Shi, F. Zhang, Z. Chen, J. Han, C. Ding, S. Chen, Z. Wang, H. Han, C. Li, *Angew. Chem. Int. Ed.* 53 (2014) 7295–7299.
- [18] Y. Li, X. Zhang, S. Jiang, Y. Li, *J. Catal.* 320 (2014) 208–214.
- [19] Z.H. Li, S.L. Feng, S.Y. Liu, X. Li, L. Wang, W.Q. Lu, *Nanoscale* 7 (2015) 19178–19183.
- [20] D.K. Zhong, M. Cornuz, K. Sivula, M. Grätzel, D.R. Gamelin, *Energy Environ. Sci.* 4 (2011) 1759–1764.
- [21] P. Zhang, T. Wang, X.X. Chang, L. Zhang, J.L. Gong, *Angew. Chem. Int. Ed.* 55 (2016) 5851–5855.
- [22] F. Malara, F. Fabbri, M. Marelli, A. Naldoni, *ACS Catal.* 6 (2016) 3619–3628.
- [23] W. Li, J. Li, X. Wang, S. Luo, J. Xiao, Q. Chen, *Electrochim. Acta* 56 (2010) 620–625.
- [24] S.C. Petitto, E.M. Marsh, G.A. Carson, M.A. Langell, *J. Mol. Catal. A: Chem.* 281 (2008) 49–58.
- [25] M. Schulze, M. Lorenz, N. Wagner, E. Gülow, *Fresenius J. Anal. Chem.* 365 (1999) 106–113.
- [26] K. Sivula, F. Le Formal, M. Grätzel, *ChemSusChem* 4 (2011) 432–449.
- [27] L. Steier, I. Herraiz-Cardona, S. Gimenez, F. Fabregat-Santiago, J. Bisquert, S.D. Tilley, M. Grätzel, *Adv. Funct. Mater.* 24 (2014) 7681–7688.
- [28] B. Klahr, S. Gimenez, F. Fabregat-Santiago, T. Hamann, J. Bisquert, *J. Am. Chem. Soc.* 134 (2012) 4294–4302.
- [29] A. Annamalai, P.S. Shinde, T.H. Jeon, H.H. Lee, H.G. Kim, W. Choi, J.S. Jang, *Sol. Energy Mater. Sol. Cells* 144 (2016) 247–255.
- [30] B. Klahr, S. Gimenez, F. Fabregat-Santiago, J. Bisquert, T.W. Hamann, *J. Am. Chem. Soc.* 134 (2012) 16693–16700.
- [31] D. Monllor-Satoca, M. Bartsch, C. Fabrega, A. Genc, S. Reinhard, T. Andreu, J. Arbiol, M. Niederberger, J.R. Morante, *Energy Environ. Sci.* 8 (2015) 3242–3254.
- [32] G.M. Carroll, D.R. Gamelin, *J. Mater. Chem. A* 4 (2016) 2986–2994.
- [33] F. Malara, A. Minguzzi, M. Marelli, S. Morandi, R. Psaro, V. Dal Santo, A. Naldoni, *ACS Catal.* 5 (2015) 5292–5300.
- [34] R. Liu, Z. Zheng, J. Spurgeon, X. Yang, *Energy Environ. Sci.* 7 (2014) 2504–2517.
- [35] T.L. Villarreal, R. Gómez, M. Neumann-Spallart, N. Alonso-Vante, P. Salvador, *J. Phys. Chem. B* 108 (2004) 15172–15181.